



Interfacial fracture resistance of the joint of a solid oxide fuel cell glass–ceramic sealant with metallic interconnect



Chih-Kuang Lin^{a,*}, Wei-Hong Shiu^{a,b}, Si-Han Wu^b, Chien-Kuo Liu^b, Ruey-Yi Lee^b

^a Department of Mechanical Engineering, National Central University, Jhong-Li 32001, Taiwan

^b Physics Division, Institute of Nuclear Energy Research, Lung-Tan 32546, Taiwan

HIGHLIGHTS

- Interfacial fracture energy of SOFC sealant/interconnect joint is determined.
- Interfacial fracture energy at 650 °C–800 °C is much larger than that at 25 °C.
- Maximum fracture energy takes place at 700 °C due to a crack bridging mechanism.
- A 1000-h thermal aging treatment enhances the fracture energy at 700 °C–800 °C.
- Chromate layer and glass–ceramic/chromate interface are the typical cracking path.

ARTICLE INFO

Article history:

Received 14 February 2014

Received in revised form

16 March 2014

Accepted 18 March 2014

Available online 26 March 2014

Keywords:

Planar solid oxide fuel cell

Glass–ceramic sealant

Metallic interconnect

Interfacial fracture energy

Thermal aging

ABSTRACT

Interfacial cracking resistance of a joint between a glass–ceramic sealant (GC-9) and interconnect stainless steel (Crofer 22 H) for planar solid oxide fuel cells is investigated. Interfacial fracture energy is measured at room temperature to 800 °C using a four-point bending test technique. A heat treatment of 100 h or 1000 h at 800 °C is applied for studying the thermal aging effect. Results show the variation trend of interfacial fracture energy with temperature is similar for all given material conditions. Interfacial fracture energy increases with temperature to reach a peak value at 700 °C and then drops at temperature above 700 °C. A 100-h aging treatment does not change the interfacial fracture energy significantly, compared to the non-aged condition. The 1000 h-aged joint, however, has greater interfacial fracture energy than the non-aged and 100 h-aged joints at 700 °C–800 °C. Two types of cracking path in the interior of fracture surface are identified. Firstly, delamination takes place at the interface between the glass–ceramic substrate and chromate layer. Secondly, cracking occurs within the chromate layer. However, for the 1000 h-aged joints tested at 700 °C–800 °C, fracture at the highly oxidized, peripheral regions takes place within the glass–ceramic layer.

© 2014 Elsevier B.V. All rights reserved.

1. Introduction

Solid oxide fuel cells (SOFCs) utilize solid ceramics as the electrolyte and electrode and operate at high temperatures. The high operating temperature enables SOFCs to have a superior efficiency of energy conversion and an advantage in flexibility of fuel needed, compared to other fuel cells. Two major configuration designs are being developed for SOFC, namely tubular and planar cells. Advantageous features of planar SOFCs (pSOFCs) over the tubular ones include easier fabrication, lower operation temperature, and higher power density. In particular, for anode-supported pSOFCs with a thinner electrolyte, the operation temperature can be lowered to

less than 800 °C and the ohmic loss is also reduced, compared to the electrolyte-support configuration. In practical applications of pSOFC, multiple cells are assembled to form a stack and make a serial connection in the electric loop to generate a high voltage and power. As a result, interconnects play an important role in structural and electrical connection of unit cells. During the stacking process and operation, hermetic sealants are needed to maintain gas tight between components in pSOFCs. When a rigid type of sealing is applied to pSOFC stacks, joining glass–ceramic sealants to metallic interconnects is very common. Sealants are typically applied in a pSOFC stack at the following locations: (a) cell to metal frame; (b) metal frame to metal interconnect; (c) frame/interconnect pair to electrically insulating spacer; (d) stack to base manifold plate [1]. Seals at locations (b) and (d) can be regarded as a joint of glass–ceramic sealant and metallic interconnect.

* Corresponding author. Tel.: +886 3 426 7340; fax: +886 3 425 4501.

E-mail addresses: t330014@cc.ncu.edu.tw, t330014@gmail.com (C.-K. Lin).

Significant thermal stresses can be developed in an SOFC system due to mismatch of coefficient of thermal expansion (CTE) between components and temperature gradients during cyclic operation [2,3]. Accordingly, thermal stresses are generated in the joint between glass–ceramic sealant and metallic interconnect in pSOFC stacks [1–3]. Thermal stresses at such a joint may cause failure of sealing with excessive deformation and/or debonding, leading to gas leakage and degradation of cell performance. Therefore, it is necessary to investigate the mechanical properties of such a joint for assessing the structural integrity and durability of a pSOFC stack. The mechanical properties in the interface of a joint between two dissimilar materials do not belong to those of either material. Any interaction between the glass–ceramic and metal may influence the mechanical properties of their joint. Although a few studies have investigated the mechanical properties of the joint of SOFC glass–ceramic sealant/metallic interconnect, they are mainly focused on the bonding strength and creep behavior [4–11]. Little literature, in particular experimental work, is related to the interfacial cracking resistance of such a joint in pSOFCs [12–14].

In terms of mechanical strength of a joint, the interface between dissimilar materials is where cracks usually initiate and propagate so that it may be the weakest part in a joint [12]. The interfacial cracking resistance is important particularly for the joints involving brittle materials such as glass–ceramic sealants because of the pre-existing defects [12]. In the studies of Malzbender et al. [13,14], interfacial fracture energy was investigated for the joint of SOFC components using a four-point bending test technique at room temperature in air. Sandwich specimens with glass–ceramic sealant between two interconnect steel strips were used to determine the interfacial fracture energy for the glass–ceramic/interconnect joint [13,14]. Their results revealed that the interfacial fracture energy increases with increasing annealing/aging time [13,14]. Those results of Malzbender et al. [13,14] were determined only at room temperature. However, pSOFC stacks work at high temperatures and there is lack of study related to the interfacial fracture energy of such joints at operating temperature. Thus, it is still needed to investigate the interfacial fracture energy of the glass–ceramic/interconnect joint at SOFC working temperature.

As hermetic sealants are usually weaker than other components in an SOFC system, a systematic investigation of mechanical properties of joints between glass–ceramic sealants and metallic interconnects at both room temperature and operating temperature is necessary for design of a reliable pSOFC stack. As part of a series of studies [10,11,15–21] on the mechanical properties of glass–ceramic sealants and metallic interconnects for pSOFCs, the aim of this study is to investigate the interfacial cracking resistance between a BaO–B₂O₃–Al₂O₃–SiO₂ glass–ceramic sealant (GC-9) and a ferritic-stainless-steel interconnect (Crofer 22 H) for pSOFC applications. Interfacial fracture energy of the glass–ceramic/metallic interconnect joint is evaluated at room temperature to 800 °C. In order to study the effect of thermal aging on the interfacial fracture energy, some joint samples are tested after aging at 800 °C in air for various lengths of time.

2. Experimental procedures

2.1. Materials and specimens

In order to investigate the interfacial fracture energy of glass–ceramic/interconnect joint, a notched sandwich specimen configuration for bending test is used in this study, as shown in Fig. 1. The glass–ceramic sealant, designated as GC-9, used to join the two metallic coupons is a novel BaO–B₂O₃–Al₂O₃–SiO₂ glass which has recently been developed at the Institute of Nuclear Energy Research

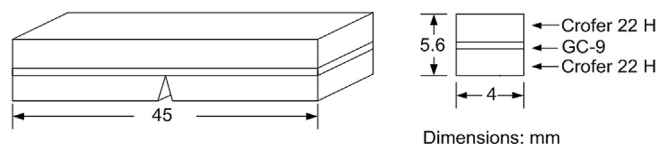


Fig. 1. Geometry of sandwich joint specimen for four-point bending test.

(INER) for pSOFCs. Chemical composition of the patented GC-9 glass–ceramic in mol% includes 34 BaO, 9.5 B₂O₃, 4.5 Al₂O₃, 34 SiO₂, 12 CaO, 5 La₂O₃, and 1 ZrO₂ [22]. Relevant mechanical properties of the GC-9 glass–ceramic have been reported previously [15–18]. The GC-9 glass sealant shows good thermal properties, chemical compatibility and stability, and hermetic properties for use in pSOFCs [23–27]. The GC-9 glass has a glass transition temperature (T_g) and softening temperature (T_s) of 668 °C and 745 °C, respectively [15]. The GC-9 glass was made by mixing the constituent oxide powders followed by melting at 1550 °C for 10 h. After melting, it was poured into a mold preheated to 680 °C to produce GC-9 glass ingots. The GC-9 glass ingots were then annealed at 680 °C for 8 h and cooled down to room temperature. GC-9 glass powders were made by crushing the as-cast glass ingots and sieving with 325-mesh sieves. The average size of the glass powder is 45 μm. Slurries were then made by adding into the GC-9 powders the desired amounts of solvent (alcohol), binder (ethyl celluloid), and plasticizer (polyethylene glycol).

The metallic coupons of the joint specimens are made of a newly developed commercial ferritic stainless steel, Crofer 22 H (ThyssenKrupp VDM GmbH, Germany), which is a heat-resistant alloy developed for pSOFC interconnects. Chemical composition of the Crofer 22 H alloy in wt% includes 22.93 Cr, 1.94 W, 0.51 Nb, 0.43 Mn, 0.21 Si, 0.08 La, 0.07 Ti, 0.02 Cu, 0.02 Al, 0.014 P, 0.007 C, <0.002 S, and balance of Fe. Relevant mechanical properties of the Crofer 22 H alloy can be found in a previous study [20]. A large steel plate supplied by the vendor was cut into small ones having plane dimensions of 5 cm × 5 cm and a thickness of 2.5 mm for making sandwich joint specimens. No surface treatment is given to the steel plates such that their bonding areas remain as received surface condition. The arithmetical mean roughness (R_a) of the steel plate surface is around 0.25 μm, as measured by a surface roughness tester. Before joining process, each steel plate was cleaned with alcohol.

A slurry of GC-9 was spread on one side of each steel plate for making the metallic interconnect/glass–ceramic/metallic interconnect joint (Fig. 1). The as-assembled sandwich plates were then put into a furnace to dry the slurry at 80 °C. The sandwich plates were then sintered under a compressive load through appropriate heat treatments. In order to simulate a practical assembling process of a pSOFC stack, the applied compressive load is 12.25 kPa. In the sintering process, the joined plates were firstly held at 500 °C for 1 h to remove the binder and plasticizer, heated to 900 °C, and held for 4 h. The heating rate at each step is 5 °C min^{−1}. After the joining process, thickness of the glass–ceramic layer is about 0.6 mm. Each sandwich plate was then cut by a diamond saw into rectangular bars of dimensions of 4 mm × 5.6 mm × 45 mm (Fig. 1) for four-point bending test. Machining direction is along the 45-mm-length longitudinal direction. A spark-erosion wire cutting technique was used to generate a notch in one of the metallic coupons of each specimen. The notch tip is in the proximity of the interface. As the spark-erosion cutting wire has a diameter of 0.2 mm, the radius of the notch tip is around 0.1 mm. Some specimens were heat treated in air at 800 °C for 100 h or 1000 h to investigate the effects of thermal aging on the interfacial fracture energy.

2.2. Mechanical testing

A four-point bending technique after Charalambides et al. [28] and Malzbender et al. [13,14] is applied in the current study for determining the interfacial fracture energy of the given glass–ceramic/metallic interconnect joint at various temperatures. Four-point bending tests were performed using a commercial closed-loop servo-hydraulic material test machine attached with a furnace. The flexural loading fixture (Fig. 2) with a 20-mm inner loading span and a 40-mm outer loading span is made of alumina in order to perform tests at 25 °C, 650 °C, 700 °C, 750 °C, and 800 °C. Each specimen was heated to the specified temperature at a heating rate of 6 °C min^{−1}, and then held at the specified temperature for 3 min before applying the mechanical load. The load was applied under displacement control with a displacement rate of 0.005 mm s^{−1}. For each test, a digital charge-coupled-device (CCD) camcorder with a high magnification macro-lens is applied to observe and record the cracking process in the specimen during loading. A visible window is made on the front door of the furnace for this purpose. The load–displacement relationship was recorded for each test to calculate the interfacial fracture energy. The recorded videography is applied to identifying the critical load in the load–displacement curve at the onset of interfacial cracking. In order to obtain reproducible data for each test parameter, five specimens are repeatedly tested at each temperature for both aged and non-aged conditions.

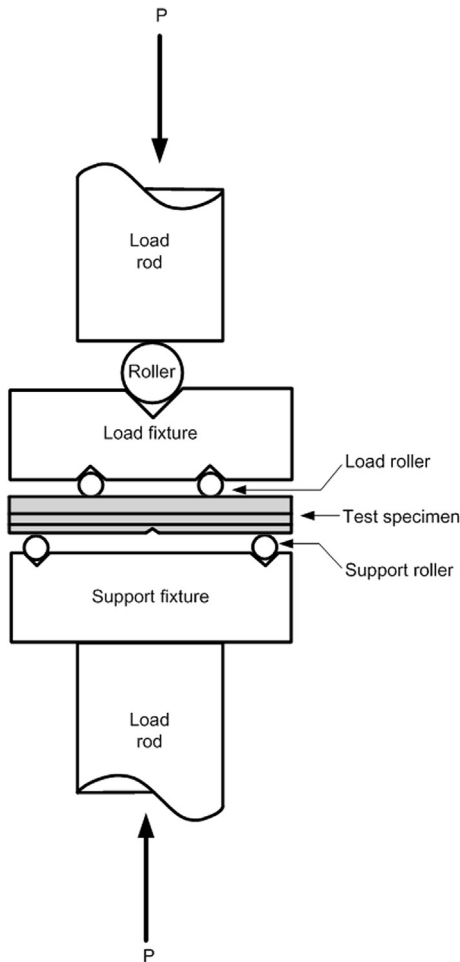


Fig. 2. Schematic of four-point bending test setup.

In this study, each layer of the multi-layered specimen is assumed to be isotropic and behave in a linear elastic manner for calculating fracture energy. As shown in Fig. 2, the interfacial crack is subjected to a constant bending moment in a four-point bending test as long as it remains within the inner loading span. An analytical calculation of strain energy release rate can be obtained for interfacial cracks located between the inner loading points [28]. The strain energy release rate is in a steady state when the crack length is much larger than the thickness of the upper layer of the specimen [28]. Furthermore, the strain energy release rate is independent of crack length, and the crack length measurement is unnecessary for such a four-point bending test [29,30]. The value of the strain energy release rate can be derived from the difference in strain energy in the uncracked and cracked specimens [13,28,29,31]. Based on Euler–Bernoulli beam theory for a uniform isotropic beam under a plane strain condition, the strain energy is [13,28]

$$U = \frac{(1 - \nu^2)M^2}{2wEI} \quad (1)$$

where U is the strain energy, E is the Young's modulus, I is the moment of inertia of the beam cross section, w is the width of the specimen, ν is the Poisson's ratio, and M is the bending moment between the two inner loading points and is equal to $Pa/2$. P is the applied load and a is the distance between the outer and inner loading points.

The fracture energy of interfacial cracking, G_{int} , between layer j and $j + 1$ of a n -layered composite beam under a plane strain condition is given as [31]

$$G_{\text{int}} = \frac{P^2 a^2}{8w} \left(\frac{1}{\Sigma_s} - \frac{1}{\Sigma_c} \right) \quad (2)$$

where Σ_s and Σ_c are beam stiffness of the debonded and intact regions, respectively, of the specimen and P is the applied load corresponding to the onset of the propagation of interfacial crack. The composite beam stiffness is defined as [31]

$$\Sigma = \int_{\text{beam}} \frac{E(y)}{1 - \nu^2(y)} y^2 dA \quad (3)$$

where y is the location relative to the neutral axis, $E(y)$ and $\nu(y)$ are the Young's modulus and the Poisson's ratio, respectively, at location y , and A is the cross-sectional area of the composite beam. The layers are numbered from 1 at the bottom to n at the top. For the intact regions in the specimen, the position of the neutral axis from the bottom surface, y_{in} , is defined as [13]

$$y_{\text{in}} = \frac{\sum_{i=1}^n E_i w_i t_i \left(2 \sum_{k=1}^{i-1} t_k + t_i \right)}{2 \sum_{i=1}^n E_i w_i t_i} \quad (4)$$

For the debonded regions in the specimen, the position of the neutral axis from the bottom surface, y_{deb} , is given as [13]

$$y_{\text{deb}} = \frac{\sum_{i=1}^j E_i w_i t_i \left(2 \sum_{k=1}^{i-1} t_k + t_i \right)}{2 \sum_{i=1}^j E_i w_i t_i} \quad (5)$$

where E_i is the Young's modulus, w_i is the width, and t_i is the thickness for layer i of a rectangular cross section in the specimen.

In Eqs. (2) and (3), the interfacial fracture energy can be determined once the geometrical parameters, material properties, and the critical load corresponding to the onset of interfacial cracking are known. The Young's moduli of Crofer 22 H and GC-9 at room temperature to 800 °C, given in Refs. [17,20], are used to determine the interfacial fracture energy for the given GC-9/Crofer 22 H joint in the current study. The Poisson's ratio of both Crofer 22 H and GC-9 is assumed to be 0.3. Given a testing temperature, the critical load corresponding to the onset of interfacial cracking is the key parameter in determining the interfacial fracture energy. Therefore, how to determine the critical load in the load–displacement curve is very important.

Usually, two types of interfacial crack extension take place during four-point bending test: (1) stable propagation, also known as crack creeping and (2) unstable propagation, also called crack bursting [31]. Which type of propagation takes place is attributed to the variation of interfacial fracture energy with position of interfacial crack and to the factors dependent on the beam stiffness [31]. During crack creeping for an interfacial crack within the inner loading span, the interfacial fracture energy is independent of crack length and is almost constant. Therefore, the applied load does not change with increasing displacement in the load–displacement curve [13,30,31]. When crack bursting occurs, a load drop can be found in the load–displacement curve. The load corresponding to the onset of crack propagation in Eq. (2) is defined as [31]

$$P = \sqrt{P_1 P_2} \quad (6)$$

where P_1 and P_2 are the maximum and minimum load during the load drop, namely the load before and after the load drop, respectively.

2.3. Microstructural analysis

After four-point bending test, fracture surfaces of selected specimens were observed with an optical microscope and a scanning electron microscope (SEM) to characterize the cracking path. SEM was also employed to examine the interfacial morphology between the glass–ceramic sealant and metallic interconnect. An energy dispersive spectrometer (EDS) module attached to the SEM was used for composition analysis in order to determine various elemental distributions on the fracture surface.

3. Results and discussion

3.1. Interfacial cracking resistance of non-aged glass–ceramic/metallic interconnect joint

There are two glass–ceramic/steel interfaces in the joint specimen of Fig. 1. To distinguish the position, the interface near the notch is called the first interface, and the other is called the second interface thereafter. Fig. 3(a) shows the load–displacement relationship for a four-point bending test conducted at room temperature. In the outlined region, the applied load becomes stable and is independent of the increasing displacement. There is a significant difference in the stiffness of specimen, namely slope of the load–displacement curve, between the outlined region and the preceding linear portion. As shown in Fig. 3(b), it is found that the crack which initiates at the notch penetrates through the glass–ceramic layer and then propagates along the second interface. The interfacial fracture energy is thus determined using the constant load value in the plateau. When the crack leaves the inner loading span after the crack creeping region, the applied load increases again due to a termination of crack propagation [13,28,30,31].

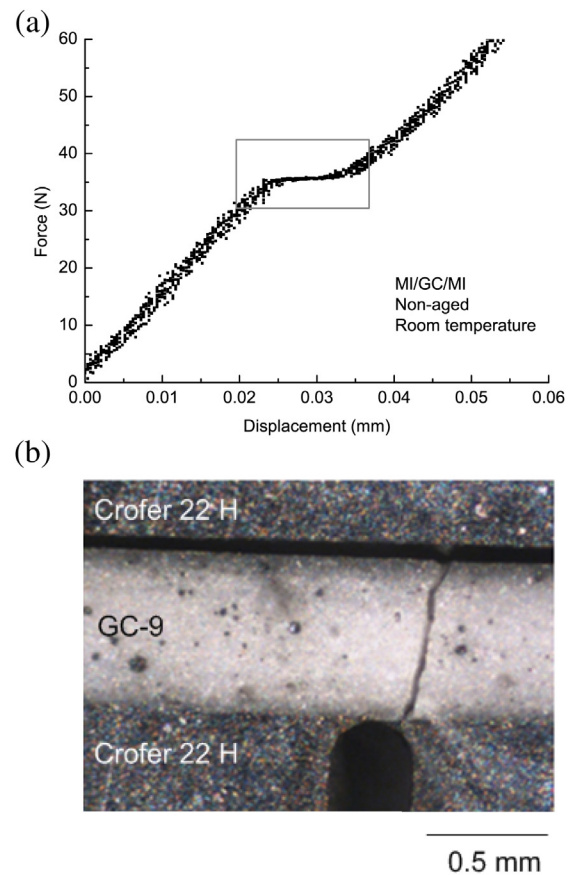


Fig. 3. Representative results of non-aged joint tested at room temperature: (a) load–displacement relationship; (b) side view of specimen cracking at the outlined stage.

There are two load drops in a load–displacement curve obtained at 650 °C (Fig. 4(a)). Cracking at the first and second load drop observed by the digital camcorder is shown in Fig. 4(b) and (c), respectively. Each load drop is attributed to initiation of a crack at the notch root, followed by penetration through the glass–ceramic layer and propagation along the second interface. Because growth of an interfacial crack takes place during the first load drop, it is classified as a bursting type of crack extension [31]. Equation (6) is thus applied to the first load drop to determine the critical load and then the interfacial fracture energy.

As shown in Fig. 5(a) for a test conducted at 700 °C, the load initially increases with increasing displacement until a maximum value is reached. Then, the load decreases as a result of initiation of cracks at the notch root, penetrating through the glass–ceramic layer and propagating along the second interface, as shown in Fig. 5(b). The load becomes stable when the crack length is much larger than the thickness of the intact layer of the specimen [28]. Consequently, the stable load value in the outlined region of Fig. 5(a) is applied to calculating the interfacial fracture energy.

The load–displacement relationship for a joint specimen tested at 750 °C is shown in Fig. 6(a). The curve is similar to that for a specimen tested at 700 °C (Fig. 5(a)). Videography (Fig. 6(b)) also shows that cracks penetrate through the glass–ceramic layer and grow along the second interface after initiation at the notch root. The load–displacement relationship and cracking pattern for 750 °C are similar to that for 700 °C such that the load used to calculate the interfacial fracture energy is also taken from the stable region outlined in Fig. 6(a).

As shown in Fig. 7(a), two distinct plateaus are outlined in the load–displacement curve obtained for a test performed at 800 °C.

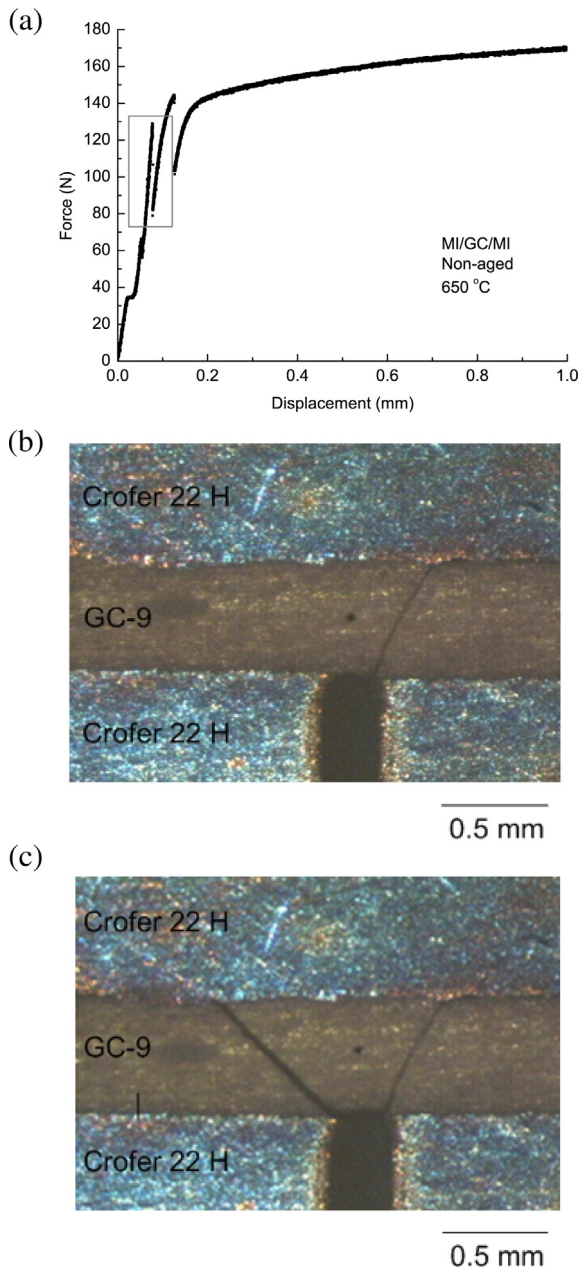


Fig. 4. Representative results of non-aged joint tested at 650 °C: (a) load–displacement relationship; (b) side view of specimen cracking at the first load drop; (c) side view of specimen cracking at the second load drop.

At the first plateau, it is observed that crack propagates along the first interface (Fig. 7(b)). Then, the crack penetrates through the glass–ceramic layer and grows along the second interface (Fig. 7(c)), corresponding to the second plateau in Fig. 7(a). For comparison purpose, only the interfacial fracture energy at the second interface is calculated for 800 °C as cracking only takes place at the second interface for the other given testing temperatures. Note that in all of the load–displacement curves described above, a small load step takes place around 35 N. This might be caused by backlash of the fixture and jig in the test machine, as no videography evidence is found for a speculation that it might correspond to the onset of crack formation at the notch tip.

The experimentally determined interfacial fracture energy (average value and a standard deviation) at various temperatures

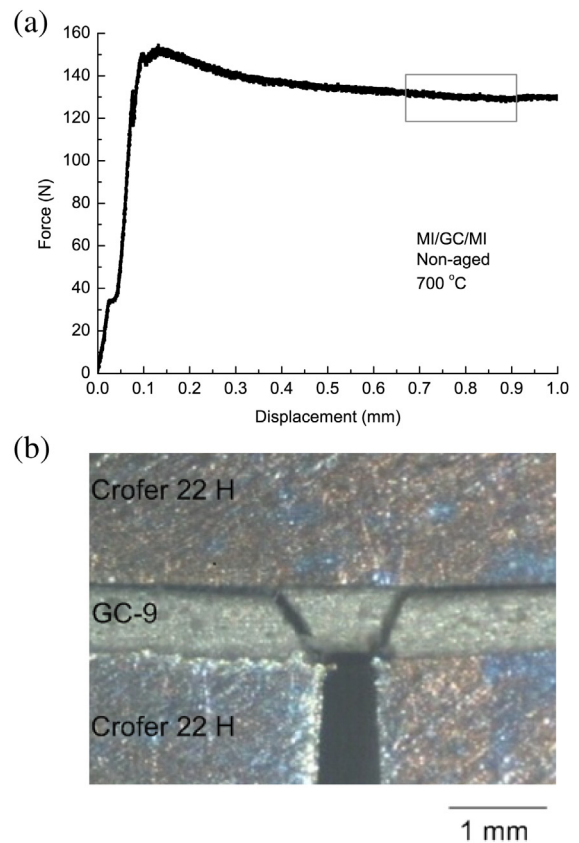


Fig. 5. Representative results of non-aged joint tested at 700 °C: (a) load–displacement relationship; (b) side view of specimen cracking at the outlined stage.

for the non-aged GC-9/Crofer 22 H joint is listed in Table 1. As expected, the interfacial fracture energy at high temperatures (650 °C–800 °C) is significantly larger than that at room temperature, as materials become tougher and softer. As shown in Table 1, the interfacial fracture energy increases from room temperature to reach a maximum value at 700 °C followed by a continuous decrease until 800 °C. As described in Section 2.1, the glass transition temperature (T_g) and softening temperature (T_s) of the GC-9 glass–ceramic are at 668 °C and 745 °C, respectively [15]. As 700 °C is higher than T_g , a greater viscosity takes place and causes a bridging phenomenon (Fig. 8) within the crack at the glass–ceramic/steel interface. It needs more energy to overcome the bridging barriers for driving the interfacial crack to propagate. Note that such bridging phenomenon is observed for all the non-aged specimens tested at 700 °C but it is never found at other testing temperatures. The interfacial fracture energy decreases at 750 °C and it is attributed to a softening behavior of GC-9 as 750 °C is higher than T_s . The interfacial fracture energy decreases further at 800 °C as a result of a greater extent of softening for GC-9. Apparently, viscosity of the glassy phase plays a very important role in the interfacial fracture resistance of the GC-9/Crofer 22 H joint at high temperatures.

3.2. Effect of thermal aging

As described above, two sets of joint specimen were thermally aged at 800 °C, one for 100 h and the other for 1000 h. For the 100 h-aged joint specimens, interfacial cracking only takes place along the second interface during four-point bending test at all given testing temperatures. A creeping type of crack extension is

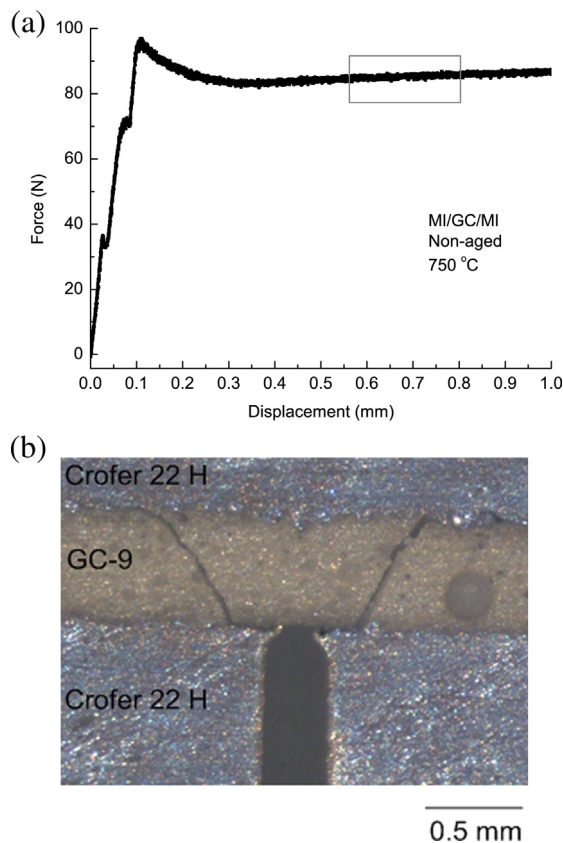


Fig. 6. Representative results of non-aged joint tested at 750 °C: (a) load–displacement relationship; (b) side view of specimen cracking at the outlined stage.

observed at room temperature, 700 °C, and 800 °C, while a bursting type of crack extension is observed at 650 °C and 750 °C. The critical load for the onset of interfacial cracking in the 100 h-aged joint specimens is determined in a similar way to that described in the previous section. Accordingly, the interfacial fracture energy at various temperatures for the 100 h-aged GC-9/Crofer 22 H joint is then determined and given in Table 1. Similar to that of the non-aged joint, the 100 h-aged interfacial fracture energy at high temperatures is significantly greater than that at room temperature and has a peak value at 700 °C.

For the 1000 h-aged joint specimens, interfacial crack extension is also found to take place only at the second interface for all given testing temperatures. A creeping type of crack extension is observed at all given testing temperature except 650 °C at which a bursting type of crack extension is observed. The critical load for the onset of interfacial cracking is determined for the 1000 h-aged joint specimens according to the aforementioned methods. Table 1 also lists the interfacial fracture energy at various temperatures for the GC-9/Crofer 22 H joint after 1000 h of thermal aging. The 1000 h-aged interfacial fracture energy also shows an increasing trend from room temperature to 700 °C and then gradually decreases until 800 °C. Again, the high-temperature interfacial fracture energy is considerably larger than that at room temperature.

Fig. 9 shows a comparison of the interfacial fracture energy for the non-aged, 100 h-aged, and 1000 h-aged glass–ceramic/steel joints at various testing temperatures. In Fig. 9, each symbol indicates the average value and the attached error bar represents the standard deviation. Note that the interfacial fracture energy values given in Fig. 9 all correspond to an interfacial crack extension

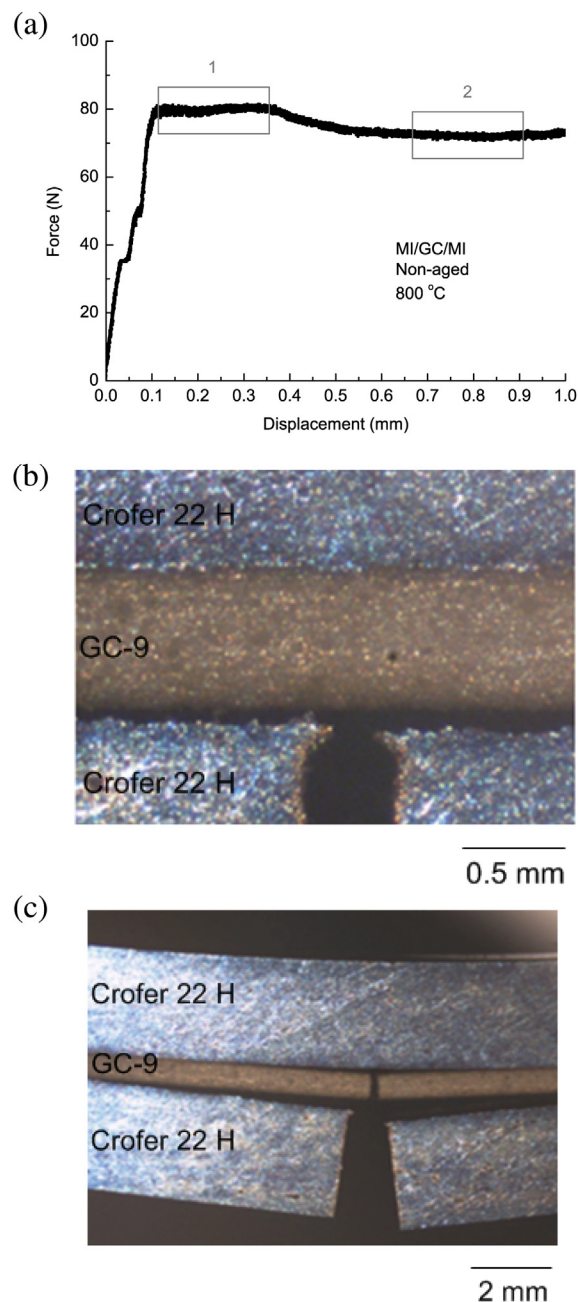


Fig. 7. Representative results of non-aged joint tested at 800 °C: (a) load–displacement relationship; (b) side view of specimen cracking at outlined stage 1; (c) side view of specimen cracking at outlined stage 2.

Table 1

Fracture resistance of glass–ceramic/interconnect steel joint at various temperatures.

Test temperature (°C)	Interfacial fracture energy, G_{int} (J m ⁻²)		
	Non-aged	100 h-aged	1000 h-aged
25	3.01 ± 0.22	2.93 ± 0.19	3.07 ± 0.26
650	46.27 ± 2.02	44.38 ± 10.55	33.80 ± 5.14
700	55.53 ± 3.06	54.69 ± 1.48	62.01 ± 3.14
750	42.97 ± 1.32	39.02 ± 2.77	55.99 ± 0.70
800	29.98 ± 2.22	29.63 ± 1.05	36.94 ± 2.28

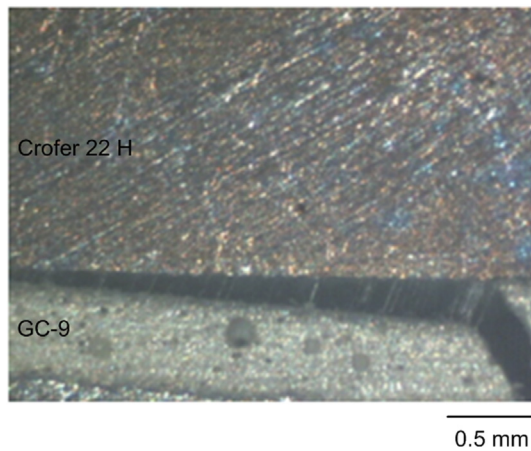


Fig. 8. Bridging phenomenon within a crack at the interface of a non-aged joint tested at 700 °C.

taking place at the second interface in the sandwich joint specimen. As shown in Fig. 9, the interfacial fracture energy of the non-aged and 100 h-aged conditions is comparable at all given temperatures, but it shows a much larger value for the 1000 h-aged condition at high temperatures. However, trends in the variation of interfacial fracture energy with temperature for both aged and non-aged conditions are similar; i.e. the interfacial fracture energy at high temperatures is significantly greater than that at room temperature and has a peak value at 700 °C. As described above, this is attributed to a change of viscosity with temperature for the given GC-9 glass–ceramic sealant, even though T_g and T_s of the 100 h-aged and 1000 h-aged conditions increase a little bit respectively from that of the non-aged condition due to a greater extent of crystallization [17,18]. Again, it indicates the glassy phase plays an important role in determining the interfacial fracture resistance of the GC-9/Crofer 22 H joint even though crystallization takes place in the GC-9 sealant during thermal aging treatment at 800 °C [17,18]. Detailed microstructural features such as pores, microvoids, crystalline phases, and glassy phase for all the given thermally aged conditions of the GC-9 glass–ceramic sealant are given in Ref. [18].

Although the trends in the curves of variously aged conditions are similar (Fig. 9), the interfacial fracture energy of the

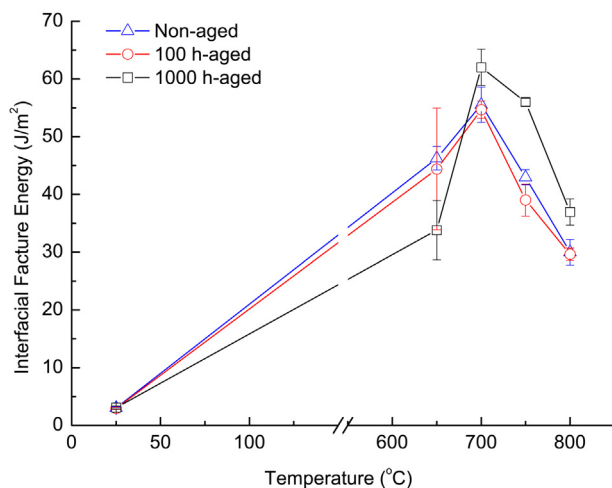


Fig. 9. Variation of interfacial fracture energy with temperature for non-aged, 100 h-aged, and 1000 h-aged joints.

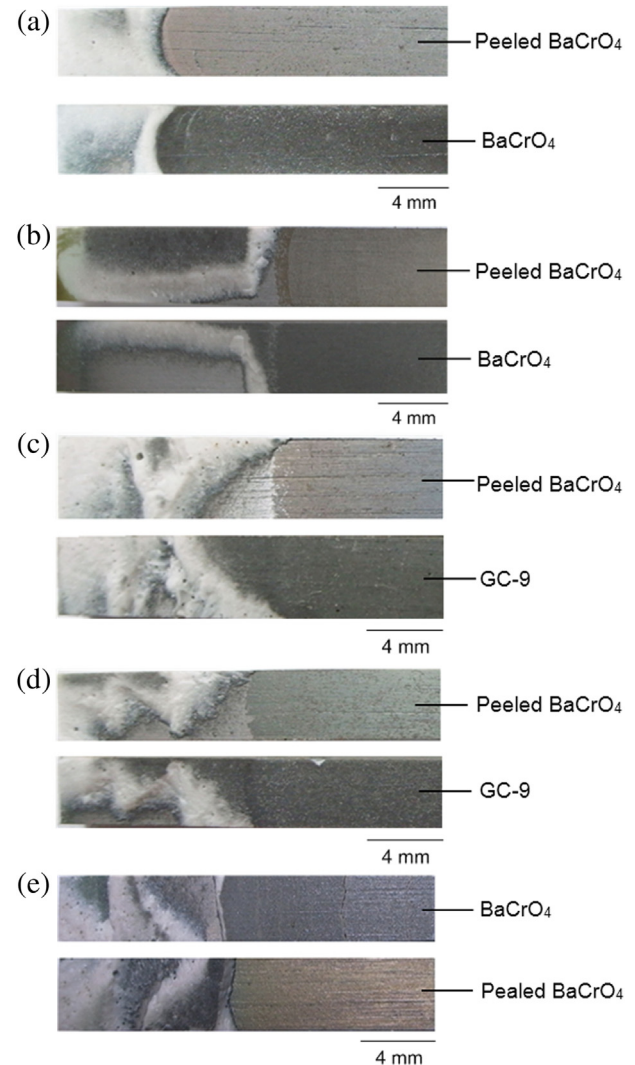


Fig. 10. Failure patterns of non-aged joints tested at: (a) room temperature; (b) 650 °C; (c) 700 °C; (d) 750 °C; (e) 800 °C.

1000 h-aged condition is clearly different from that of other aged conditions except at room temperature. At room temperature, there is no significant difference in interfacial fracture energy among the given three aged conditions. As listed in Table 1, the average interfacial fracture energy at room temperature in the present study is about 3 J m^{-2} regardless of the aged condition. The thermal aging effect on the room-temperature interfacial cracking resistance in the current study is different from that in the studies of Malzbender et al. [13,14]. In the studies of Malzbender et al. [13,14], the fracture energy of a sandwich joint between a barium–calcium–aluminosilicate glass–ceramic and Crofer 22 APU steel increases with thermal aging time at 800 °C. In those studies, the average room-temperature fracture energy for a 24 h-aged, 120 h-aged, 500 h-aged, and 1000 h-aged condition is 12, 23, 56, and 53 J m^{-2} , respectively [13,14]. Note that the fracture path in those cases is essentially located within the glass–ceramic layer rather than at the interface between the glass–ceramic and interconnect steel [14]. This might explain why the trend of thermal aging effect in Malzbender et al. [13,14] is different from that in the present work in which cracking at room temperature all takes place along the glass–ceramic/steel interface. Detailed results and discussion of the fractography analysis are given in next section. The average

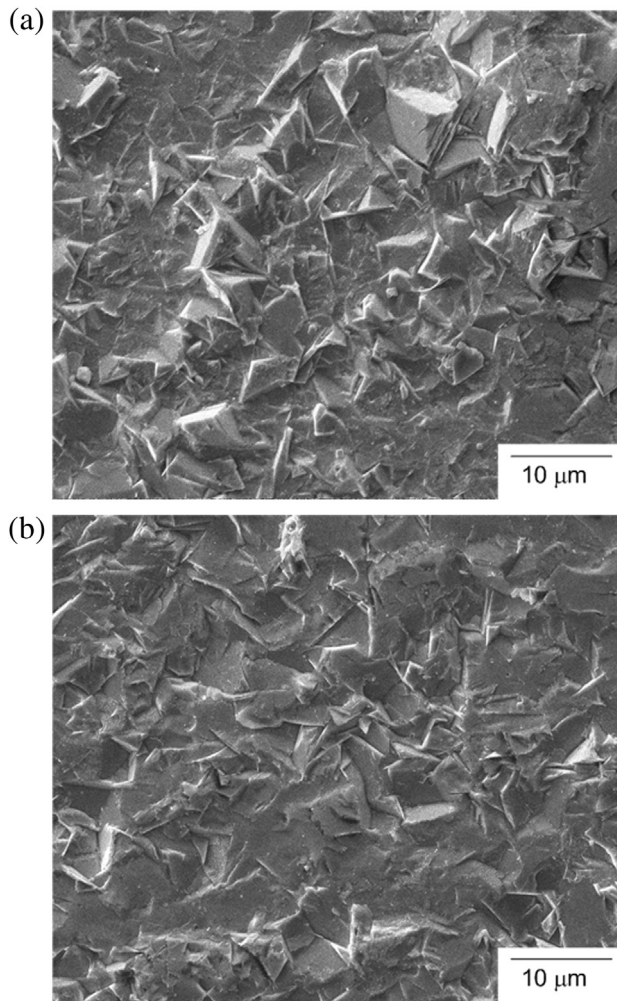


Fig. 11. Fracture surfaces of the non-aged specimen shown in Fig. 10(a): (a) a high-magnification SEM micrograph of an area in the upper micrograph of Fig. 10(a); (b) a high-magnification SEM micrograph of an area in the lower micrograph of Fig. 10(a).

room-temperature fracture energy (3 J m^{-2}) of the present study is significantly lower than those ($12\text{--}53 \text{ J m}^{-2}$) of Malzbender et al. [13,14]. If cracking path is the only factor responsible for such a difference in room-temperature fracture energy, it implies that the interfacial oxide layers between the glass–ceramic sealant and interconnect steel provide a much weaker fracture path than does the glass–ceramic substrate itself. In this regard, how to enhance the bonding characteristics at the interface between the glass–ceramic sealant and interconnect steel to increase the cracking resistance is a critical issue when applying sealing to real pSOFC stacks. However, in addition to cracking path, differences in the composition of the glass–ceramic sealant, composition and surface preparation of the interconnect steel, and bonding parameters between the current study and Malzbender et al. [13,14] are other possible reasons for the difference in the room-temperature results. As Malzbender et al. [13,14] did not report any high-temperature results, it is not sure whether cracks in their joints would propagate along the glass–ceramic/steel interface or within the glass–ceramic layer at SOFC operating temperature.

As shown in Fig. 9, the 1000 h-aged interfacial fracture energy is smaller than that of the other two aged conditions at 650°C . As T_g increases for a longer aging time and a greater extent of crystallization [17,18], the 1000 h-aged glass–ceramic sealant is expected to become more brittle than the 100 h-aged and non-aged ones at

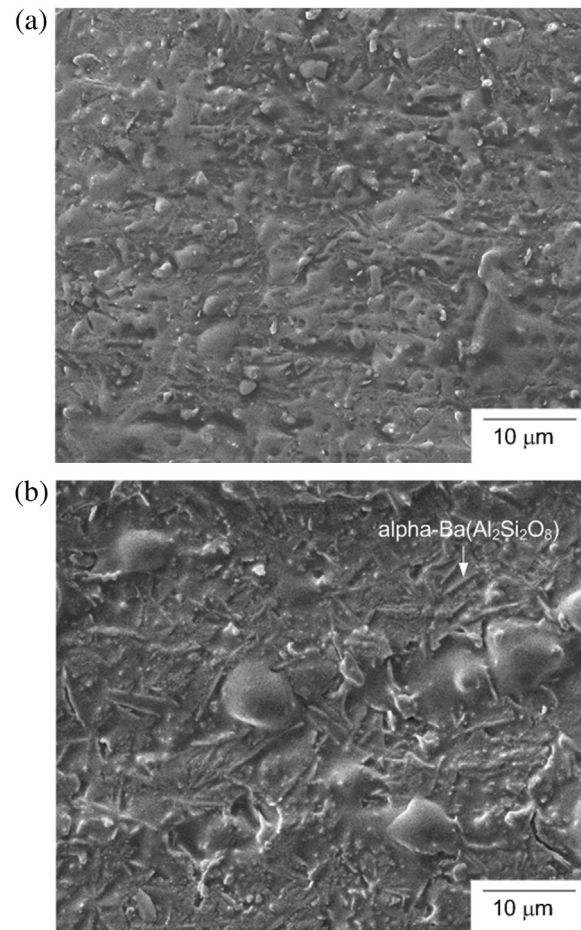


Fig. 12. Fracture surfaces of the non-aged specimen shown in Fig. 10(c): (a) a high-magnification SEM micrograph of an area in the upper micrograph of Fig. 10(c); (b) a high-magnification SEM micrograph of an area in the lower micrograph of Fig. 10(c).

650°C . The 1000 h-aged interfacial fracture energy is larger than the 100 h-aged and non-aged ones at temperature of 700°C and above. It is attributed to a greater viscosity effect of the residual glassy phase in the glass–ceramic sealant because T_g shifts closely toward 700°C for a longer aging time [17].

3.3. Failure analysis

The high-temperature joining mechanism of the GC-9 glass–ceramic sealant with Crofer 22 H alloy involves formation of two oxide layers, namely a chromia (Cr_2O_3) layer on the surface of Crofer 22 H and a chromate (BaCrO_4) layer on the surface of GC-9 [10]. A spinel ($(\text{Cr,Mn})_3\text{O}_4$) layer is formed between these two oxide layers [10]. Fig. 10 shows the failure patterns in the non-aged joint specimens tested at various temperatures. Due to symmetry of the joint specimen with respect to the central notch, only a half of the broken joint specimen is shown in Fig. 10 for each case. Note in Fig. 10, both sides of fracture surface are shown for each half joint specimen and the notch is located at the right edge of each micrograph. In other words, the interfacial crack propagates stably from the right edge toward the left during test. As a fast breaking action is taken to separate the unbroken portion after test for observing the fracture surfaces, the unstable fast fracture surface near the left edge is quite rough and will not be discussed. Only the stable propagation region in the right portion of each micrograph is observed in details for discussion. It is found that delamination

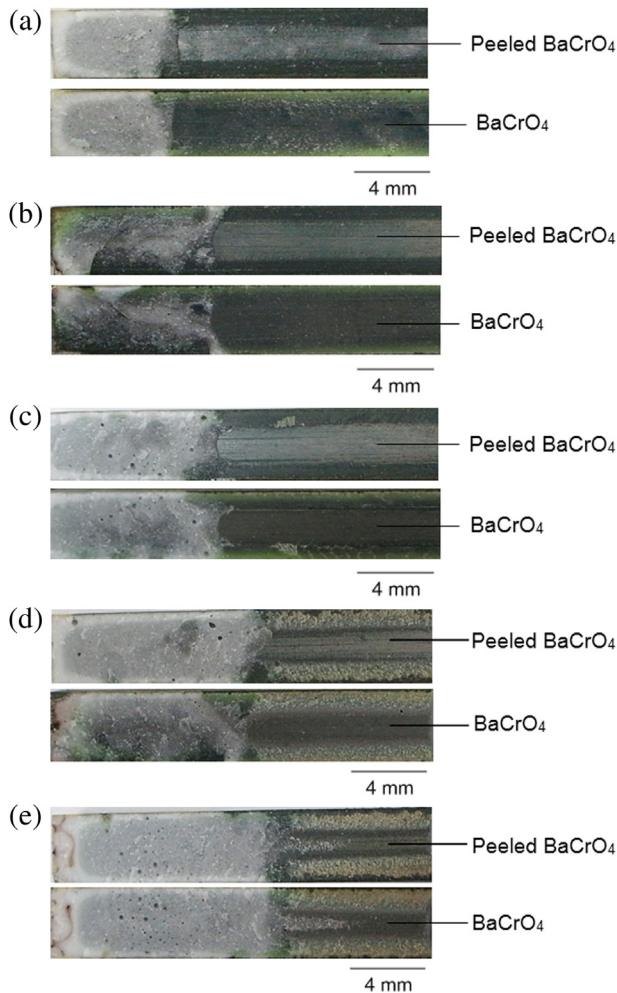


Fig. 13. Failure patterns of 1000 h-aged joints tested at: (a) room temperature; (b) 650 °C; (c) 700 °C; (d) 750 °C; (e) 800 °C.

occurs uniformly at the stable cracking region in each optical micrograph, and some of the delaminated regions are further observed and analyzed using SEM and EDS.

For the non-aged joint specimen tested at room temperature, Fig. 11(a) and (b) shows the high-magnification SEM micrographs of a selected flat cracking region in each of the upper and lower micrographs of Fig. 10(a), respectively. Protrusions and dent-like features are observed in Fig. 11(a) and (b). By means of EDS analysis, the three major chemical elements detected in Fig. 11(a) and (b) are Ba, Cr, and O. It indicates that the interfacial crack propagates mainly within a chromate layer. Such SEM fractography features are also found in the non-aged joint specimen tested at 650 °C, indicating a similar interfacial cracking path at both room temperature and 650 °C.

Fig. 12(a) and (b) shows the SEM micrographs corresponding to the upper and lower OM micrographs of Fig. 10(c), respectively, for a non-aged specimen tested at 700 °C. An amorphous phase with needle-shape imprints is found in Fig. 12(a). In addition to the amorphous phase, needle-shape crystalline phases (α -Ba($\text{Al}_2\text{Si}_2\text{O}_8$)) are observed in Fig. 12(b). The amorphous phase is likely responsible for the bridging phenomenon observed at 700 °C (Fig. 8). As Cr, Ba, and O elements are detected by EDS analysis, the amorphous phase is mixed with chromate. For the oxide layers formed between GC-9 and Crofer 22 H, the chromate layer is adjacent to GC-9. As needle-shape crystalline phases are found in

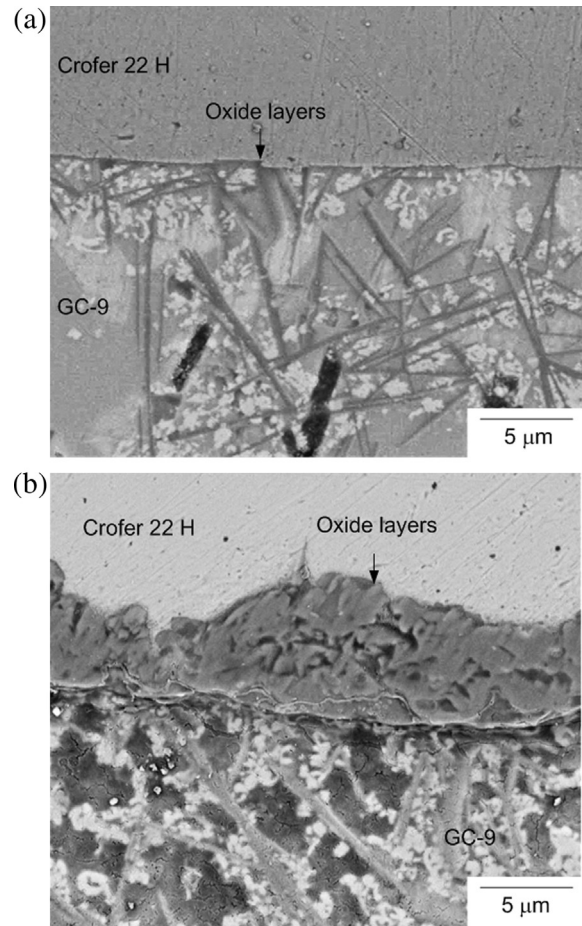


Fig. 14. SEM micrographs of a cross section of the interface between GC-9 and Crofer 22 H at variously aged conditions in BSE mode: (a) non-aged; (b) 1000 h-aged.

Fig. 12(b) and there is no crystalline phase in Fig. 12(a), it implies the crack propagates mostly along the interface between the GC-9 glass–ceramic substrate and chromate layer. It indicates that the chromate with needle-shape imprints (Fig. 12(a)) is caused by separation of α -Ba($\text{Al}_2\text{Si}_2\text{O}_8$) phases from the chromate. A similar interfacial cracking path between the GC-9 and chromate layers is also observed for the non-aged joint specimen tested at 750 °C. For non-aged joint specimens tested at 800 °C, the amorphous phase is observed, and there are no needle-shape crystalline phases in both upper and lower fracture surfaces of Fig. 10(e). Consequently, the delamination takes place within the chromate layer.

For the 100 h-aged joint specimens, the fracture path and fractography features are generally similar to those of the non-aged specimens at each given testing temperature. This is consistent with the mechanical testing results that the interfacial fracture energy of the non-aged and 100 h-aged conditions is comparable at all given testing temperatures. Fig. 13 shows the failure patterns in the 1000 h-aged joint specimens tested at various temperatures. As shown in each micrograph of Fig. 13, the stable cracking area at the right portion of the fracture surface can be distinguished into two colors, namely the interior and peripheral regions. A wide, thick oxide region at peripheral edges of the fracture surface is found in each 1000 h-aged joint specimen (Fig. 13). However, no such features are observed in the non-aged micrographs, as shown in Fig. 10. It is caused by growth of oxide layer during thermal aging treatment. A greater extent of oxidization is expected to take place

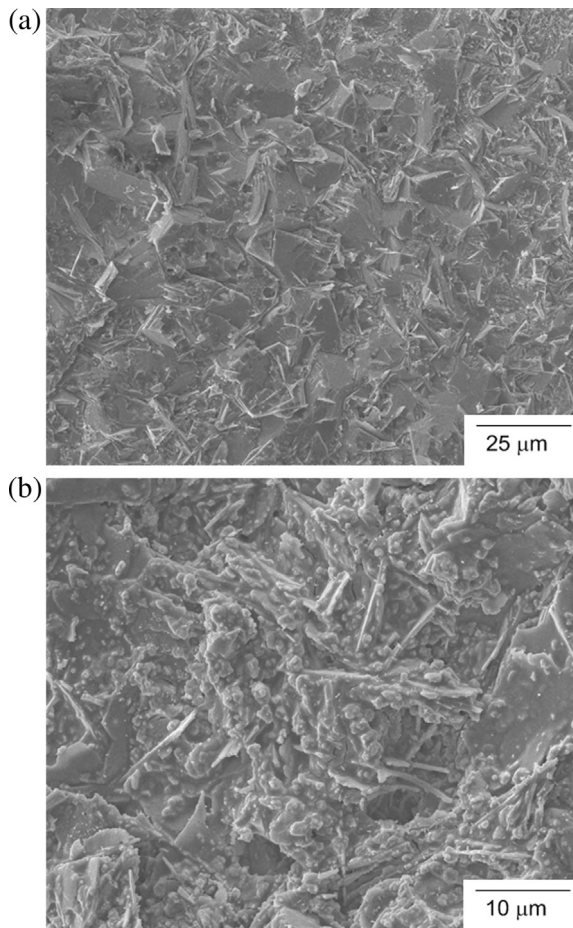


Fig. 15. High-magnification SEM micrographs of an area at the periphery of fracture surface for 1000 h-aged joints tested at: (a) 650 °C; (b) 700 °C.

at the periphery of a 1000 h-aged joint specimen, compared to the interior region inside the specimen. Cross-sectional microstructures of the interface between GC-9 and Crofer 22 H at peripheral regions for variously aged conditions are shown in the SEM micrographs of Fig. 14 with a back-scattered electron (BSE) mode. The oxide layer shown in Fig. 14(b) for a 1000 h-aged joint is significantly greater than that of a non-aged joint shown in Fig. 14(a). It indicates that the oxide layer becomes much thicker after a long-term thermal aging treatment.

Protrusions and dent-like features as shown in Fig. 11 are also found in the interior region for the 1000 h-aged joint specimen tested at all given temperatures. Again, it indicates the interfacial cracking path in the interior region is located within the chromate layer for the 1000 h-aged joint specimens, as also evidenced by EDS analysis. Fig. 15(a) shows a representative high-magnification SEM micrograph at the periphery in both sides of fracture surface for a 1000 h-aged joint specimen tested at 650 °C (Fig. 13(b)). As protrusions and dent-like features are observed in Fig. 15(a), it indicates stable cracking at the periphery takes place mostly within the chromate layer, which is similar to that in the interior. Such microstructures at the periphery of the fracture surface are also found for the 1000 h-aged specimen tested at room temperature (Fig. 13(a)). Fig. 15(b) shows a representative high-magnification SEM micrograph at the periphery in both sides of fracture surface for a 1000 h-aged joint specimen tested at 700 °C (Fig. 13(c)). Needle-shape crystalline phases (α -Ba($\text{Al}_2\text{Si}_2\text{O}_8$)) are observed in Fig. 15(b) indicating that stable cracking proceeds within the GC-

9 substrate at the periphery. Similarly, fracture takes place within the glass–ceramic layer at the peripheral edges of the 1000 h-aged specimens when tested at 750 °C and 800 °C (Fig. 13(d) and (e)). Note that for the 1000 h-aged joint specimens the interfacial cracking path in the interior is located within the chromate layer at all given testing temperatures, as described above. Such a difference in cracking path between the peripheral and interior regions is likely associated with the superior interfacial cracking resistance of the 1000 h-aged joint specimens to that of the non-aged and 100 h-aged ones at 700 °C–800 °C. Also note that the enhanced oxide layer at the periphery in the 100 h-aged joint specimen is not as wide as that in the 1000 h-aged joint specimen due to a shorter heat treatment time. In this regard, the fractography features and interfacial cracking resistance are comparable between the 100 h-aged and non-aged joint specimens.

4. Conclusions

- (1) A four-point bending test technique with in-situ videography observation for measuring the interfacial cracking resistance between glass–ceramic sealant and metallic interconnect at room temperature to 800 °C is developed in the present study.
- (2) The interfacial fracture energy at 650 °C–800 °C is significantly larger than that at room temperature for each given aged condition, as materials become tougher and softer. The interfacial fracture energy of as-assembled GC-9/Crofer 22 H joint increases from room temperature to reach a maximum value at 700 °C followed by a continuous decrease until 800 °C. The maximum value at 700 °C is attributed to a crack bridging mechanism.
- (3) Thermal aging treatment at 800 °C for 100 or 1000 h does not significantly change the variation trend of interfacial fracture energy of GC-9/Crofer 22 H joint with temperature; i.e. a peak value still takes place at 700 °C. The interfacial fracture energy is comparable for the non-aged and 100 h-aged joints at all given testing temperatures, while the 1000 h-aged joint shows a greater interfacial cracking resistance than the non-aged and 100 h-aged ones at temperatures of 700 °C–800 °C.
- (4) For non-aged and 100 h-aged glass–ceramic/interconnect steel joints, crack propagates along the interface between the chromate layer and glass–ceramic substrate when tested at 700 °C and 750 °C, while it propagates within the chromate layer at room temperature, 650 °C, and 800 °C.
- (5) A wide, thick oxide region at peripheral edges of the fracture surface is found in the 1000 h-aged joint specimens. For 1000 h-aged joints, crack propagates within the chromate layer in the interior at each given testing temperature. However, it propagates within the glass–ceramic layer at the periphery when tested at 700 °C–800 °C.

Acknowledgments

This work was supported by the Institute of Nuclear Energy Research under Contract No. 102-2001-INER-031.

References

- [1] P.A. Lessing, J. Mater. Sci. 42 (2007) 3465–3476.
- [2] C.-K. Lin, T.-T. Chen, Y.-P. Chyou, L.-K. Chiang, J. Power Sources 164 (2007) 238–251.
- [3] C.-K. Lin, L.-H. Huang, L.-K. Chiang, Y.-P. Chyou, J. Power Sources 192 (2009) 515–524.
- [4] E.V. Stephens, J.S. Vetrano, B.J. Koeppel, Y. Chou, X. Sun, M.A. Khaleel, J. Power Sources 193 (2009) 625–631.
- [5] F. Smeacetto, M. Salvo, M. Ferraris, V. Casalegno, P. Asinari, A. Chrysanthou, J. Eur. Ceram. Soc. 28 (2008) 2521–2527.

- [6] Y.-S. Chou, J.W. Stevenson, P. Singh, J. Power Sources 184 (2008) 238–244.
- [7] Y.-S. Chou, J.W. Stevenson, P. Singh, J. Power Sources 185 (2008) 1001–1008.
- [8] J. Malzbender, Y. Zhao, J. Mater. Sci. 47 (2012) 4342–4347.
- [9] J. Malzbender, Y. Zhao, Fuel Cells 12 (2012) 47–53.
- [10] C.-K. Lin, J.-Y. Chen, J.-W. Tian, L.-K. Chiang, S.-H. Wu, J. Power Sources 205 (2012) 307–317.
- [11] C.-K. Lin, K.-L. Lin, J.-H. Yeh, S.-H. Wu, R.-Y. Lee, J. Power Sources 245 (2014) 787–795.
- [12] A. Muller, W. Becker, D. Stolten, J. Hohe, Eng. Fract. Mech. 73 (2006) 99–1008.
- [13] J. Malzbender, R.W. Steinbrech, L. Singheiser, J. Mater. Res. 18 (2003) 929–934.
- [14] J. Malzbender, R.W. Steinbrech, L. Singheiser, P. Batfalsky, Ceram. Eng. Sci. Proc. 26 (2005) 285–291.
- [15] H.-T. Chang, C.-K. Lin, C.-K. Liu, J. Power Sources 189 (2009) 1093–1099.
- [16] H.-T. Chang, C.-K. Lin, C.-K. Liu, J. Power Sources 195 (2010) 3159–3165.
- [17] H.-T. Chang, C.-K. Lin, C.-K. Liu, S.-H. Wu, J. Power Sources 196 (2011) 3583–3591.
- [18] C.-K. Lin, K.-L. Lin, J.-H. Yeh, W.-H. Shiu, C.-K. Liu, R.-Y. Lee, J. Power Sources 241 (2013) 12–19.
- [19] Y.-T. Chiu, C.-K. Lin, J.-C. Wu, J. Power Sources 196 (2011) 2005–2012.
- [20] Y.-T. Chiu, C.-K. Lin, J. Power Sources 198 (2012) 149–157.
- [21] Y.-T. Chiu, C.-K. Lin, J. Power Sources 219 (2012) 112–119.
- [22] C.-K. Liu, T.-Y. Yung, K.-F. Lin, R.-Y. Lee, T.-S. Lee, Glass–Ceramic Sealant for Planar Solid Oxide Fuel Cells, United States Patent No. 7,897,530 B2, 2011.
- [23] C.-K. Liu, T.-Y. Yung, K.-F. Lin, in: Proceedings of the Annual Conference of the Chinese Ceramic Society 2007 (CD-ROM), 2007 (in Chinese).
- [24] C.-K. Liu, T.-Y. Yung, S.-H. Wu, K.-F. Lin, in: Proceedings of the MRS-Taiwan Annual Meeting 2007 (CD-ROM), 2007 (in Chinese).
- [25] C.-K. Liu, T.-Y. Yung, K.-F. Lin, in: Proceedings of the Annual Conference of the Chinese Ceramic Society 2008 (CD-ROM), 2008 (in Chinese).
- [26] C.-K. Liu, K.-C. Tsai, K.-F. Lin, S.-H. Wu, T.-Y. Yung, in: Proceedings of the Annual Conference of the Chinese Ceramic Society 2009 (CD-ROM), 2009 (in Chinese).
- [27] C.-K. Liu, T.-Y. Yung, K.-F. Lin, R.-Y. Lee, S.-H. Wu, ECS Trans. 25 (2009) 1491–1500.
- [28] P.G. Charalambides, J. Lund, A.G. Evans, R.M. McMeeking, J. Appl. Mech. 56 (1989) 77–82.
- [29] L.R. Katipelli, A. Agarwal, N.B. Dahotre, Mater. Sci. Eng. A 289 (2000) 34–40.
- [30] H. Hirakata, T. Yamada, Y. Nobuhara, A. Yonezu, K. Minoshima, Eng. Fract. Mech. 77 (2010) 803–818.
- [31] L. Zou, Y. Huang, C. Wang, J. Eur. Ceram. Soc. 24 (2004) 2861–2868.